

A Virtual Sensor for Integral Tire Force Estimation using Tire Model-less Approaches and Adaptive Unscented Kalman Filter

Manuel Acosta, Stratis Kanarachos and Michael E. Fitzpatrick

School of Mechanical, Aerospace and Automotive Engineering, Coventry University, Coventry, U.K.

Keywords: Virtual Sensors, Tire Force Estimation, Unscented Kalman Filter, Adaptive Kalman Filter, Neural Networks.

Abstract: In this paper, a novel approach to estimate the longitudinal, lateral and vertical tire forces is presented. The innovation lies a) in the proposition of a modular state estimation architecture that lessens the tuning effort and ensures the filter's stability and b) in the estimation of the longitudinal velocity relying only on the wheel speed information. The longitudinal forces are estimated using an Adaptive Random-Walk Linear Kalman Filter. The lateral forces per axle are estimated by combining an Adaptive Unscented Kalman filter and Neural Networks. The individual tire lateral forces are inferred from the axle lateral forces using the vertical load proportionality principle. The individual tire vertical forces are estimated using a steady-state weight transfer approach, in which the roll stiffness distribution is considered. The state estimator is implemented in *Simulink*® and simulations are carried out in the vehicle dynamics simulation software *IPG CarMaker*®. The virtual sensor is tested in aggressive and steady-state maneuvers, exhibiting in both cases a remarkable performance.

1 INTRODUCTION

Latest advances found in the literature indicate that Modern Automotive Control Systems (e.g Drift Control) will be required to maximize the vehicle safety at the limits of adhesion (Acosta et al., 2016; Gray et al., 2012; Velenis et al., 2011; Chakraborty et al., 2011). In order to guarantee an accurate and robust actuation of these systems, it is necessary to have a precise knowledge of a large number of vehicle states, such as the vehicle body slip or the longitudinal wheel slip. Nevertheless, direct measurement of these signals is in most situations neither cost-effective nor reliable and thus state estimation approaches are required.

Despite some attempts found in literature employing vehicle model-less approaches (Hrgetic et al., 2011; Klier et al., 2008), the standard methodology to estimate the vehicle states is to use model-based estimation techniques. Depending on the nature of the analytical equations used to model the vehicle behavior, linear or nonlinear observers are employed. The Extended Kalman Filter (*EKF*) and the Unscented Kalman Filter (*UKF*) are often used for nonlinear vehicle state estimation (Doumiati et al., 2012), the latter being most suitable for problems exhibiting strong nonlinearities (Doumiati et al., 2009). As the vehicle behavior depends greatly on the friction forces generated by the tires, a precise knowledge of these

forces is required in order to have a reliable estimation of the vehicle states. Tire force estimation based on tire models such as the Magic Formula or the Dugoff model (Pacejka, 2012) has been covered extensively in the literature (Doumiati et al., 2012; Antonov et al., 2011; Gao, 2010; Wenzel et al., 2006).

While tire model-based estimation is straightforward once an accurate tire model is available, the generation of a precise model is not trivial, and involves extensive experimental testing. Moreover, the outputs from the model are subjected to uncertainties due to the influence of other vehicle subsystems (e.g. elasto-kinematics from the suspension system). In order to overcome these limitations and avoid the necessity of employing a specific tire model, many authors have focused on tire model-less approaches (Acosta and Kanarachos, 2016; Hrgetic et al., 2014; Hamann et al., 2014; Albinsson et al., 2014; Cho et al., 2010). Tire model-less approaches can be grouped into *stochastic* or *random-walk* (Hrgetic et al., 2014; Hamann et al., 2014; Cho et al., 2010), *open loop* (Albinsson et al., 2014; Cho et al., 2010), and *data-based* (Acosta and Kanarachos, 2016).

When *random-walk* modeling is employed, the tire forces are treated as steady-state variables, and the time evolution of the variable is provided entirely by the measurement update stage of the filter. In order to achieve a fast response, it is necessary to assign

large weights to the corresponding terms of the process covariance matrix (Doumiati et al., 2012), with the subsequent increase in the noise level of the estimated signal. In this paper, an adaptive process covariance matrix handled by a Fuzzy Logic controller is employed to overcome this issue. In addition, while other works assume that the vehicle velocity is measurable (e.g. using a GPS system (Hamann et al., 2014; Baffet et al., 2009)) this variable is inferred from the wheel rotating speed in this work, and an adaptive *UKF* is proposed to limit the effect of the wheel speed fluctuations during hard braking. The rest of the paper is structured in the following manner.

In Section 2, relevant background about Kalman Filtering is provided, and the Linear and Unscented Kalman Filters are formulated. The structure of the virtual sensor is described in Section 3, where the models employed in the vertical, longitudinal and planar dynamics blocks are presented. Simulation results are provided in Section 4. Finally, conclusions and further research steps are discussed in Section 5.

2 BACKGROUND

2.1 Linear Kalman Filter

The state-space formulation is adopted to present the Linear Kalman Filter (*LKF*). Thus, a generic linear system can be expressed by the equations (1-2).

$$\mathbf{X}_{k+1} = \mathbf{A}_k \mathbf{X}_k + \mathbf{B}_k \mathbf{U}_k + \mathbf{w}_k \quad (1)$$

$$\mathbf{Y}_{k+1} = \mathbf{C}_k \mathbf{X}_k + \mathbf{v}_k \quad (2)$$

The terms \mathbf{w}_k and \mathbf{v}_k are the plant and measurement noises respectively, and it is assumed that these noises can be approximated by a zero mean uncorrelated gaussian distribution (3-4).

$$\mathbf{w}_k \approx N(0, \mathbf{Q}_k) \quad (3)$$

$$\mathbf{v}_k \approx N(0, \mathbf{R}_k) \quad (4)$$

The estimation process is computed in two steps. First, the time step prediction is performed using the plant model, (5). At the same time, an initial covariance matrix $\mathbf{P}_{k+1|k}$ is computed based on the plant covariance matrix \mathbf{Q} , (6).

- Prediction:

$$\hat{\mathbf{X}}_{k+1|k} = \mathbf{A}_k \hat{\mathbf{X}}_{k|k} + \mathbf{B}_k \mathbf{U}_k \quad (5)$$

$$\mathbf{P}_{k+1|k} = \mathbf{A}_k \mathbf{P}_{k|k} \mathbf{A}_k^T + \mathbf{Q}_k \quad (6)$$

During the second step, the initial estimates $\hat{\mathbf{X}}_{k+1|k}$ are corrected using the measurement vector \mathbf{Y}_k and the Kalman gain \mathbf{K}_{k+1} .

- Measurement Correction:

$$\mathbf{K}_{k+1} = \mathbf{P}_{k+1|k} \mathbf{H}_k^T [\mathbf{H}_k \mathbf{P}_{k+1|k} \mathbf{H}_k^T + \mathbf{R}_k]^{-1} \quad (7)$$

$$\hat{\mathbf{X}}_{k+1|k+1} = \hat{\mathbf{X}}_{k+1|k} + \mathbf{K}_{k+1} [\mathbf{Y}_k - \mathbf{H}_k \hat{\mathbf{X}}_{k+1|k}] \quad (8)$$

$$\mathbf{P}_{k+1|k+1} = [\mathbf{I} - \mathbf{K}_{k+1} \mathbf{H}_k] \mathbf{P}_{k+1|k} \quad (9)$$

Finally, the relative importance of the process model (prediction step) or the measured variables (measurement correction) on the estimation is adjusted by the selection of the process and measurement covariance matrices \mathbf{Q} and \mathbf{R} .

2.2 Unscented Kalman Filter

The Unscented Kalman Filter (*UKF*) is employed in problems that exhibit strong nonlinearities and has been exploited in previous works to handle the vehicle nonlinear behavior (Antonov et al., 2011; Doumiati et al., 2009). As occurred in the linear case, the state-space formulation is used, and a generic nonlinear system is modeled by expressions (10-11).

$$\mathbf{X}_{k+1} = \mathbf{f}(\mathbf{X}_k, \mathbf{U}_k) + \mathbf{w}_k \quad (10)$$

$$\mathbf{Y}_{k+1} = \mathbf{h}(\mathbf{X}_k, \mathbf{U}_k) + \mathbf{v}_k \quad (11)$$

The filter is based on the Unscented Transformation (*UT*), which offers a statistical alternative to the analytical linearization carried out in the Extended Kalman Filter (*EKF*). A small set of deterministically selected sigma points are propagated through the system and the system nonlinearities are inferred from the statistics of these points. The spread of the sigma points is determined by the selection of the scaling parameters α and κ , which are related by expression (12), (Rhudy and Gu, 2013; Wan and Van Der Merwe, 2000).

$$\lambda = \alpha^2(L + \kappa) - L \quad (12)$$

Where the length of the state vector is denoted by L . In this paper, the plant and measurement noises are considered additive, and thus the formulation of the *UKF* is reduced to the formulation of the standard or unaugmented *UKF* (Rhudy and Gu, 2013). The matrix of sigma points is formed using the equation (13), where the number of rows is given by L and the number of columns corresponds to $2L + 1$.

$$\chi_k = \left[\hat{\mathbf{X}}_{k|k}, \hat{\mathbf{X}}_{k|k} + \sqrt{\Theta \mathbf{P}_{x,k|k}}, \hat{\mathbf{X}}_{k|k} - \sqrt{\Theta \mathbf{P}_{x,k|k}} \right] \quad (13)$$

Where Θ is equal to $(\lambda + L)$. The matrix square root ($\sqrt{\mathbf{P}_{x,k|k}}$) is calculated using the Cholesky method, which calculates a lower triangular matrix representative of the square root, expression (14).

$$\sqrt{\mathbf{P}_{x,k|k}}\sqrt{\mathbf{P}_{x,k|k}}^T = \mathbf{P}_{x,k|k} \quad (14)$$

The sigma points are then propagated through the nonlinear system using equation (15).

$$\mathbf{X}_{k+1|k}^i = \mathbf{f}(\chi_k^i, \mathbf{U}_k) \quad (15)$$

After that, the post-transformation mean and covariance are calculated using weighted averages, (16-17).

$$\hat{\mathbf{X}}_{k+1|k} = \sum_{i=0}^{2L} \eta_i^m \mathbf{X}_{k+1|k}^i \quad (16)$$

$$\begin{aligned} \mathbf{P}_{k+1|k} &= \mathbf{Q}_k + \\ &+ \sum_{i=0}^{2L} \eta_i^c (\mathbf{X}_{k+1|k}^i - \hat{\mathbf{X}}_{k+1|k})(\mathbf{X}_{k+1|k}^i - \hat{\mathbf{X}}_{k+1|k})^T \end{aligned} \quad (17)$$

Where the weights η_i^c and η_i^m are calculated using equations (18-20).

$$\eta_0^m = \frac{\lambda}{\lambda + L} \quad (18)$$

$$\eta_0^c = \eta_0^m + 1 - \alpha^2 + \beta \quad (19)$$

$$\eta_i^c = \eta_i^m = \frac{1}{2(L + \lambda)} \quad (20)$$

The parameter β is known as the secondary scaling parameter (Rhudy and Gu, 2013). Similarly, the matrix of sigma points is propagated through the observation function (\mathbf{h}) using expression (21).

$$\mathbf{Y}_{k+1|k}^i = \mathbf{h}(\chi_k^i) \quad (21)$$

The predicted output ($\hat{\mathbf{Y}}_{k|k}$), output covariance matrix (\mathbf{P}_{k+1}^{yy}) and cross-covariance matrix (\mathbf{P}_{k+1}^{xy}) are calculated using equations (22-24).

$$\hat{\mathbf{Y}}_{k+1|k} = \sum_{i=0}^{2L} \eta_i^m \mathbf{Y}_{k+1|k}^i \quad (22)$$

$$\begin{aligned} \mathbf{P}_{k+1}^{yy} &= \mathbf{R}_k + \\ &+ \sum_{i=0}^{2L} \eta_i^c (\mathbf{Y}_{k+1|k}^i - \hat{\mathbf{Y}}_{k+1|k})(\mathbf{Y}_{k+1|k}^i - \hat{\mathbf{Y}}_{k+1|k})^T \end{aligned} \quad (23)$$

$$\mathbf{P}_{k+1}^{xy} = \sum_{i=0}^{2L} (\mathbf{X}_{k+1|k}^i - \hat{\mathbf{X}}_{k+1|k})(\mathbf{Y}_{k+1|k}^i - \hat{\mathbf{Y}}_{k+1|k})^T \quad (24)$$

The covariance matrices calculated in the previous step are then used to compute the Kalman gain (\mathbf{K}_{k+1}), equation (25).

$$\mathbf{K}_{k+1} = \mathbf{P}_{k+1}^{xy} (\mathbf{P}_{k+1}^{yy})^{-1} \quad (25)$$

Finally, the states estimated in the first stage of the filter are corrected using the expression (26), and the covariance matrix is updated with equation (27).

$$\hat{\mathbf{X}}_{k+1|k+1} = \hat{\mathbf{X}}_{k+1|k} + \mathbf{K}_{k+1} (\mathbf{Y}_{k+1} - \hat{\mathbf{Y}}_{k+1|k}) \quad (26)$$

$$\mathbf{P}_{k+1|k+1} = \mathbf{P}_{k+1|k} - \mathbf{K}_{k+1} \mathbf{P}_{k+1}^{yy} \mathbf{K}_{k+1}^T \quad (27)$$

3 OBSERVER STRUCTURE

The complete structure of the virtual sensor proposed in this work is depicted in Fig. 1. A modular approach is selected in order to achieve a better control over the individual blocks (longitudinal, vertical, and lateral force estimation), and avoid the burden of tuning an observer with a large number of states.

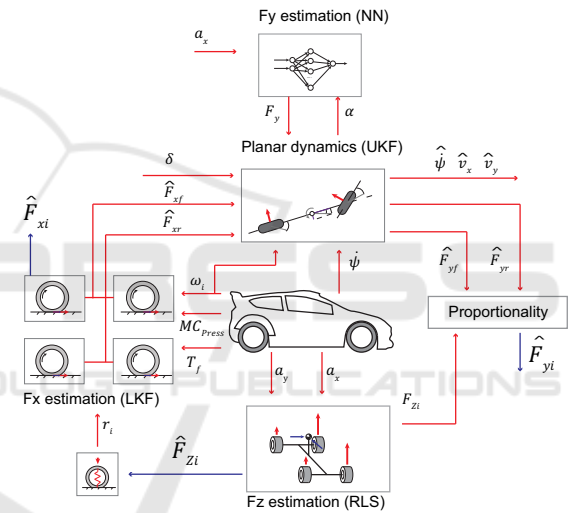


Figure 1: Modular structure of the virtual sensor for three-axis tire force and planar dynamics estimation.

The virtual sensor consists of three principal blocks: vertical force estimation block (Open loop, steady-state model), longitudinal force estimation block (Adaptive Linear Kalman Filter), and vehicle planar dynamics block (Hybrid Neural Networks - Adaptive Unscented Kalman Filter). The tire normal forces (F_{zi}) are estimated from the longitudinal (a_x) and lateral (a_y) accelerations using a quasi-static weight transfer model, refer to Section 3.1. A Recursive Least Squares (RLS) block is used to filter the noise embedded in the signals (Albinsson et al., 2014). The RLS formulation is omitted due to space limitations and can be consulted in (Young, 2011). The vertical forces are employed to calculate the wheel loaded radius (r_i) using a linear tire stiffness model, refer to Section 3.1.2. The wheel radius (r_i), wheel speed (w_i), master cylinder pressure

(MC_{press}), engine drive torque (T_f) and transmission ratio (η_i) are fed into an Adaptive Random-Walk Linear Kalman Filter to estimate the individual longitudinal forces (F_{xi}). A non-constant process covariance matrix (Q_{LKF}) is used to achieve a trade-off between dynamic response and noise rejection. The transient content of the longitudinal dynamics is captured by monitoring the rate of change of the engine revolutions ($Revs$) and the rate of change of the brake pedal position ($Pedal_{brk}$). A Fuzzy Logic controller adjusts the process covariance matrix (Q_{LKF}) based on these inputs, refer to Section 3.2.1.

The individual longitudinal forces are then lumped together at each axle and passed through the planar dynamics block. An important contribution of this work is that additional instrumentation to measure the vehicle "true" velocity (e.g. *GPS*) is not required, and the wheel rotating speeds are used instead. As these signals are not reliable during hard decelerations (wheel-lock) or hard accelerations (wheel-spin), an adaptive measurement covariance matrix (R_{UKF}) is used to adjust the relative contribution of the process model and the measured speeds depending on the driving situation, refer to Section 3.3.2.

The axle lateral forces (F_{yf}, F_{yr}) are estimated in the (*UKF*) using a data-based approach. These are inferred in a *Neural Network* structure (*NN*) from the vehicle longitudinal acceleration (a_x) and the axle lateral slips (α_i). A *UKF* propagates the modeling uncertainties through the vehicle planar dynamics model for estimating the yaw rate ($\dot{\psi}$), longitudinal velocity (v_x), and lateral velocity (v_y). Finally, the individual lateral forces (F_{yi}) are obtained using the vertical load proportionality principle (Albinsson et al., 2014). In the following subsections, the details regarding each block are presented.

3.1 Vertical Force Estimation

A quasi-static weight transfer model is used to estimate the tire vertical loads (28). In this model, the unsprung masses and the suspension dynamics are disregarded, and the front and rear roll center heights are assumed to lie on the ground. Additionally, the road is considered a completely flat surface, and thus wheel dynamic loads derived from the road irregularities are not considered. The lateral weight transfer is assumed to depend on the roll stiffness at each axle (K_{ϕ_i}), and the height (h) and the longitudinal position (l_i) of the center of gravity.

$$\begin{aligned} \hat{F}_{z_{i,j}} = & F_{z_{o_i}} \pm ma_x \frac{h}{2WB} \pm \\ & \pm a_y mh \frac{K_{\phi_i} + mh(WB - l_i)/WB}{tw_i(K_{\phi_f} + K_{\phi_r} - mh)} \end{aligned} \quad (28)$$

With $i \in \{front, rear\}$ and $j \in \{left, right\}$. For further details regarding vertical force modeling, (Pylpchuk and Chen, 2014; Doumiati et al., 2012; Doumiati et al., 2008) can be consulted.

3.1.1 Proportionality Principle

The vertical proportionality principle states that the forces generated by the tires follow a coulomb friction law, and thus can be obtained from the product of the tire-road friction coefficient and the normal load. While this approximation does not consider the load sensitivity (Pacejka, 2012) associated to the weight transfer, it provides an estimate of the individual tire forces with a reasonable accuracy and has been employed in previous works to calculate the individual tire lateral forces from the axle forces (Albinsson et al., 2014).

$$\hat{F}_{y_{i,j}} = \hat{F}_{y_i} \frac{\hat{F}_{z_{i,j}}}{\hat{F}_{z_{i,left}} + \hat{F}_{z_{i,right}}} + \Omega \quad (29)$$

The constant Ω has been added to take into account the tire asymmetric behavior derived from "ply-steer" or tire conicity effects, (Pacejka, 2012).

3.1.2 Loaded Radius

The wheel loaded radius is computed using a linear vertical stiffness model, expression (30).

$$\hat{r}_{i,j} = r_{o_i} - \frac{F_{z_{o_i,j}} - \hat{F}_{z_{i,j}}}{K_{tire}} \quad (30)$$

Where the tire radius at nominal load ($F_{z_{o_i,j}}$) is denoted by r_{o_i} , the tire vertical stiffness is K_{tire} , and the tire vertical damping is neglected.

3.2 Longitudinal Force Estimation

The tire longitudinal forces are estimated from the wheel rotating dynamics, equation (31).

$$I_{tot} \dot{\omega} = \tau - F_x r - F_z f_{res} r \quad (31)$$

In this paper, a regular front-wheel-drive vehicle with an open differential is studied, and a basic driveline architecture is considered (Kiencke and Nielsen, 2005). The torsional stiffness, damping, and rotating inertias of the drive shafts are disregarded. A perfect coupling between the engine output shaft and the gearbox input shaft is assumed when the clutch is fully engaged, and the total driveline inertia (I_{tot}) is calculated using the system of equations (32).

$$I_{tot} = \begin{cases} I_w, & \text{clutch} = 1 \\ 0.5I_{eng}\eta_{gear}^2\eta_{diff}^2 + I_w, & \text{else} \end{cases} \quad (32)$$

Where I_w is the wheel inertia, I_{eng} is the engine inertia, and η_{gear} , η_{diff} are the gear and differential (*final drive*) ratios respectively. Thus, the total inertia seen from the wheel is no longer considered constant (Hamann et al., 2014; Hrgetic et al., 2014) but adjusted based on the clutch position.

$$\tau_f = T_{eng}\eta_{gear}\eta_{diff} - T_{brk,f} \quad (33)$$

$$\tau_r = -T_{brk,r} \quad (34)$$

The net torque (τ) is calculated as the difference between the driving and the braking (T_{brk}) torques, expressions (33 - 34). Concerning the latter term, a proportional model based on the brake force distribution is employed (Hamann et al., 2014; Hrgetic et al., 2014), expressions (35-36).

$$T_{brk,f} = K_f P_f \quad (35)$$

$$T_{brk,r} = K_r P_r \quad (36)$$

The constants K_f and K_r are proportional gains that transform the brake pressure into braking torque, and account for the friction between the brake pad and the disc, and net braking force application point among other factors. The wheel rotating dynamics equation is written in state-space form using expressions (37-39),

$$\dot{x}_1 = \frac{u_1 - x_2 r - F_z f_{res} r}{I_{tot}} \quad (37)$$

$$\dot{x}_2 = 0 \quad (38)$$

$$y = x_1 \quad (39)$$

with the vector of states formed by the wheel speed and the longitudinal force ($\mathbf{x} = \{w, F_x\}$), the former being the unique system output (y). The net torque is the input to the system ($u = \{\tau\}$), and the vertical force necessary to compute the rolling resistance is introduced as a disturbance input ($d = \{F_z\}$). The rolling resistance coefficient is denoted by f_{res} , and is considered constant for simplicity. The loaded radius and total driveline inertia are modeled as time-varying parameters. Finally, the estimation of the system states is carried out using the linear Kalman Filter presented in Section 2.1.

3.2.1 Adaptive Process Covariance Matrix

The state-space formulation presented in the previous subsection treats the longitudinal force as a random-walk variable ($\dot{x} = 0$). This approach assumes that the variable remains constant during the time update stage of the filter, and relies entirely on the measurement update stage to determine how the variable evolves in time. If the fast convergence of

the random-walk variable is required during transient situations (e.g. hard braking) the process covariance terms must be assigned large weights (i.e. the assumption of quasi-static longitudinal forces is no longer valid). On the other hand, during steady-state situations in which the rate of change of the longitudinal forces is reduced (e.g. coast down), lower values of the process covariance matrix are preferred in order to reduce the noise level.

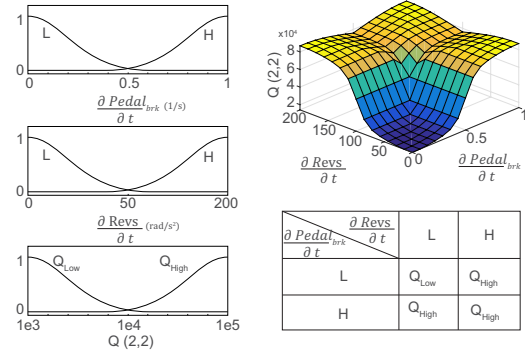


Figure 2: Fuzzy Logic Controller to handle the adaptive process covariance matrix based on the positive rate of change of the engine revolutions (rad/s^2) and the rate of change of the normalized brake pedal position ($1/s$).

An adaptive process covariance matrix is proposed to use the most appropriate values during each situation using a Fuzzy Logic Controller, Fig. 2. During constant speed situations in which the rate of change of the brake pedal is null and the engine revolutions remain constant, the second term of the process covariance matrix is assigned low values. When the engine revolutions increase abruptly (full throttle) or the brake pedal position varies (braking force build-up) the second term of the process covariance matrix is increased to achieve fast convergence of the random-walk force, Section 4.1.

3.2.2 Wheel Lock

In this paper, the braking torque is modeled as a static torque, and thus the wheel rotating dynamics expression is not suitable to estimate the longitudinal forces during severe wheel lock (the wheel rotating speed remains zero, and does not accelerate in the opposite direction). During these situations, the tire slides on the road, and the tire longitudinal force can be approximated by the product of the vertical load and the friction coefficient (40).

$$F_{x,lock} = \mu_{dyn} F_z \quad (40)$$

Where the dynamic friction coefficient (μ_{dyn}) can be calculated from the longitudinal acceleration and

the vehicle mass. The expression (41) is used to handle wheel locking situations,

$$\hat{F}_x = (1 - W)\hat{F}_{x,rot} + W\hat{F}_{x,lock} \quad (41)$$

where the factor W is null while the wheel rotating speed is above a certain threshold, and is unity when this threshold is passed. A more sophisticated strategy can be used to avoid excessive chattering if continuous wheel locking is expected (e.g. driving on gravel).

3.3 Lateral Force Estimation

The lateral forces are estimated using a vehicle planar dynamics model, expressed in state-space form by the equations (42 - 44).

$$\dot{\gamma}_1 = \frac{1}{m}(\zeta_2 \cos(\zeta_1) - F_{yf} \sin(\zeta_1) + \zeta_3) + \gamma_2 \gamma_3 \quad (42)$$

$$\dot{\gamma}_2 = \frac{1}{m}(F_{yf} \cos(\zeta_1) + \zeta_2 \sin(\zeta_1) + F_{yr}) - \gamma_1 \gamma_3 \quad (43)$$

$$\dot{\gamma}_3 = \frac{1}{I_\psi}(F_{yf} \cos(\zeta_1)l_f + \zeta_2 \sin(\zeta_1)l_f - F_{yr}l_r) \quad (44)$$

The vehicle mass is denoted by (m), the yaw inertia by (I_ψ), and the distances from the front and rear axles to the center of gravity by (l_f, l_r). The angle steered by the front wheels and the estimated axle longitudinal forces are the inputs to the system ($\zeta = \{\delta, \hat{F}_{xf}, \hat{F}_{xr}\}$). The state vector is formed by the yaw rate, longitudinal velocity, and lateral velocity ($\gamma = \{\dot{\psi}, v_x, v_y\}$). The axle lateral forces are calculated using the nonlinear tire-road friction function (45).

$$F_y = f(\alpha, a_x) \quad (45)$$

This expression depends on the longitudinal acceleration and the axle wheel slips, which are calculated using a small angle approximation (Kanarachos, 2012) with expressions (46-47).

$$\alpha_f = \delta - \frac{\gamma_1 l_f + \gamma_3}{\gamma_2} \quad (46)$$

$$\alpha_r = \frac{-\gamma_3 + \gamma_1 l_r}{\gamma_2} \quad (47)$$

Finally, equations (42-47) are integrated into an *UKF* using the formulation presented in Section 2.2.

3.3.1 Neural Networks

The axle lateral forces F_y are estimated by a Neural Networks structure, Fig. 3. The longitudinal acceleration is used in the *NN* structure in order to predict

the reduction in the lateral force during combined longitudinal and lateral excitation (force coupling), thus permitting an accurate vehicle state estimation in non-constant speed events (e.g. braking in a turn). At each time step, the *UKF* sigma-points are generated and the sigma axle slips are formed. These sigma axle slips are propagated through the *NN* to handle the tire-road friction nonlinearities and the sigma-axle lateral forces are obtained and re-injected into the *UKF*.

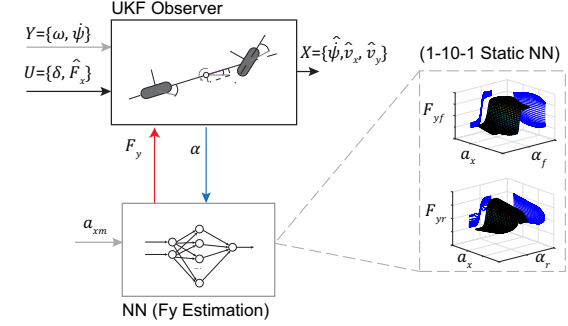


Figure 3: Unscented Kalman Filter for lateral force estimation.

The datasets necessary to train the *NN* structure were generated in *IPG-CarMaker*® using an experimentally validated compact-class vehicle model and a state-of-the-art Magic Formula 6.1 tire model (Pacejka, 2012). Open Loop aggressive maneuvers (Step steer) covering different longitudinal acceleration levels (Braking, Power On) were simulated for this purpose. Finally, the *NN* were trained in *Matlab*® using the Levenberg-Marquardt backpropagation algorithm and a 70/15/15% dataset division was selected after performing a sensitivity analysis. The stability of the *NN* structure was studied following the methodology described in (Belic, 2012). For further details, (Acosta and Kanarachos, 2016) can be consulted.

3.3.2 Adaptive Measurement Covariance Matrix

In the *UKF* described in this section, it is assumed that the longitudinal velocity measured using a *GPS* system is not available, and only the wheel speed signals can be used as a reliable measurement. Nevertheless, the wheel speed signals do not represent accurately the real vehicle velocity during hard braking or aggressive accelerations. In order to adjust the relative importance given to the process model or the measured wheel speeds, the measurement covariance matrix is varied according to the master cylinder pressure signal (MC_{press}). During driving or coast down situations, the reference velocity is calculated as the average of the non-driven (rear) wheels. Conversely, when braking occurs and the speed calculated from the non-driven wheels is prone to fluctuation (MC_{press} above

a certain threshold), the second diagonal term of the matrix R_{UKF} is increased, and the relative importance given to the measured wheel speeds is reduced. During the following stages of this research, it is intended to evaluate the suitability of this approach in estimating the reference speed (v_x) required to compute the wheel longitudinal slips, which is particularly difficult in all-wheel-drive systems during off-road driving.

4 RESULTS

The state estimator was constructed in *Simulink*® and integrated into the vehicle dynamics simulation software *IPG-CarMaker*®. The discretization time was set to 1ms, and the measurable quantities were acquired at a frequency of 100Hz using a zero-order hold block. An additive white gaussian noise model was used to incorporate the uncertainties associated with the measurement equipment in the simulation signals, (RaceLogic, 2015; Bosch, 2006), Table 1. An experimentally validated model representative of a compact-class vehicle and a Magic Formula 6.1 tire model were employed during the simulations.

Table 1: Standard deviation of the noises added to the simulation signals.

σ_{ψ} (rad/s)	σ_{a_x} (m/s ²)	σ_{a_y} (m/s ²)
0.002	0.01	0.01
σ_w (rad/s)	σ_{T_f} (Nm)	$\sigma_{MC_{press}}$ (bar)
0.1	1	1.82

The parameters of the virtual sensor are detailed in Table 2. The suspension parameters were determined in a series of steady-state Slow Increasing Steer tests.

Table 2: Virtual Sensor parameters.

l_f (m)	l_r (m)	m (kg)
0.95	1.54	1200
I_w (kgm ²)	I_{eng} (kgm ²)	t_{wf} (m)
1.05	0.064	1.45
K_{ϕ_f} (KNm/rad)	K_{ϕ_r} (KNm/rad)	t_{wr} (m)
31.74	29.30	1.45
I_{ψ} (kgm ²)	f_{res} (-)	h (m)
1668	0.01	0.66

A preliminary tuning of the *UKF* and *LKF* was carried out manually based on a systematic trial and error method. An optimized version of this observer will be presented in the future employing Swarm Intelligence optimization routines (Kanarachos et al., 2016). In the following, the results obtained with the preliminary virtual sensor are presented.

4.1 Driving / Braking Tests

The tests performed in Table 3 were simulated to evaluate the performance of the virtual sensor under longitudinal excitation.

Table 3: Acceleration and Braking tests. **FA***: Full Acceleration, **GB***: Gentle Braking, **PB***: Partial Braking, **HB***: Hard Braking.

Test	Initial speed	Drv/Brk*
#1 Acceleration	20kph	FA
#2 Braking	150kph	GB/PB/HB

The results concerning the acceleration test (#1) are depicted in Fig. 4. The vehicle accelerates hard in a straight line from first to sixth gear. The estimation of the individual longitudinal forces carried out by the *LKF* blocks is very precise and the estimated signals track very well the longitudinal force fluctuations during gear shifting. As a front-wheel-drive vehicle is employed during the simulations, the contribution of the rear forces is null during the entire test. Finally, a slight offset appears in the longitudinal velocity at high speed due to the aerodynamic drag, which is not considered in the vehicle longitudinal equilibrium equation (42). Despite this, the overall performance of the observer is remarkable, and the longitudinal velocity is well approximated by the *UKF*. A comparison between the state estimator behavior using a constant or a time-varying process covariance matrix is shown in Fig. 5.

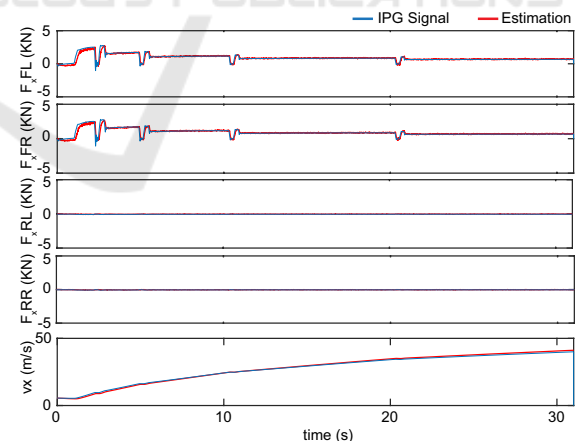


Figure 4: Longitudinal forces and longitudinal velocity (Test #1).

The details regarding the adaptive process covariance matrix were covered in Section 3.2.1. As can be observed, the *LKF* tracks with high precision the simulation signal when the term $Q_{LKF}(2,2)$ is assigned high values, with the side effect of a high noise level. On the other hand, the noise level is reduced with a low covariance value, but the dynamic response of the

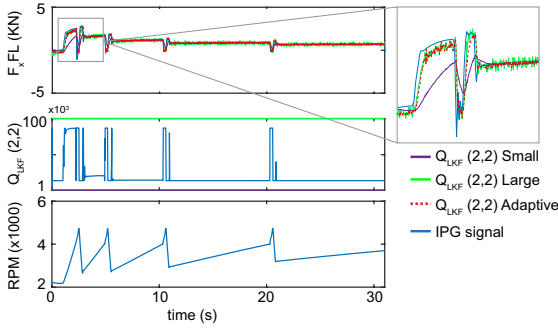


Figure 5: Comparison between constant and adaptive process covariance matrix (Test #1).

random-walk signal is very poor, and the convergence to the simulation signal is very slow. Thus, the adaptive matrix presents the best trade-off between noise rejection and dynamic response.

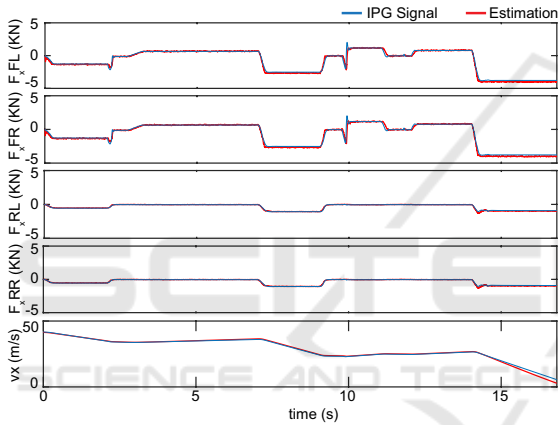


Figure 6: Longitudinal forces and longitudinal velocity (Test #2).

The results of the braking test (#2) are presented in Fig. 6. The vehicle circulates in a straight line at high speed, and a sequence of braking events (gentle, partial, hard) is performed. Although some offset is seen in the last braking input ($t \approx 14 - 16s$) the estimation of the longitudinal forces performed by the *LKF* is remarkable, and the longitudinal velocity is approximated with high accuracy by the *UKF*. This offset is caused by the wheel locking phenomena, in which the wheel rotating dynamics equations are no longer valid, and the longitudinal force is the product of the vertical force and the friction coefficient.

In order to evaluate the performance of the adaptive *UKF*, a comparison between the constant and adaptive measurement covariance term ($R_{UKF}(2,2)$) is depicted in Fig. 7. If a high value is selected, the *UKF* uses predominantly the longitudinal dynamic equilibrium equation to compute the longitudinal velocity, and any mismatch in the longitudinal forces estimated by the *LKF* is reflected in the longitudinal

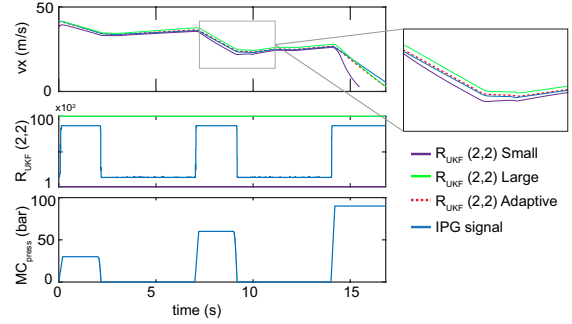


Figure 7: Comparison between constant and adaptive measurement covariance matrix (Test #2).

speed estimate (constant offset in the green curve). On the other hand, if a lower value is used (violet trace), the *UKF* relies more on the rear wheel speed and does not approximate well the real longitudinal speed during hard braking events in which abrupt wheel speed fluctuations occur. The adaptive strategy approximates with high accuracy the real longitudinal speed in spite of the wheel speed fluctuations or the model uncertainties.

4.2 Vehicle Dynamics Tests

The tests presented in Table 4 were simulated to test the performance of the virtual sensor under combined longitudinal and lateral excitation.

Table 4: Braking-in-a-turn (*BIT*) and ADAC Lane Change (*LC*) tests. **CD***: Coast down, **PB***: Partial Braking.

Test	Init. speed	A_y	Drv/Brk*
#3 ADAC LC	95kph	Limit	CD
#4 BIT	60kph	Limit	PB

For simplicity, active systems such as Anti-lock Braking System (*ABS*), Electronic Stability Program (*ESP*) or Electronic Brakeforce Distribution (*EBD*) are not considered in this work. The interaction of the state estimator with these systems will be addressed in future stages of this research.

The tire forces estimated during the execution of the Allgemeiner Deutscher Automobil-Club (*ADAC*) Lane change (#3) are portrayed in Fig. 8. This test is executed in coast down conditions, and thus the tires do not generate significant longitudinal forces. The lateral forces predicted by the virtual sensor follow closely the simulation signals, what indicates the suitability of the vertical proportionality principle to infer the individual lateral forces from the axle lateral forces. Concerning the normal forces, some discrepancies are observed in the estimates of the front axle ($t \approx 21s$). The maximum offset occurs during the second gate of the lane change, during which the

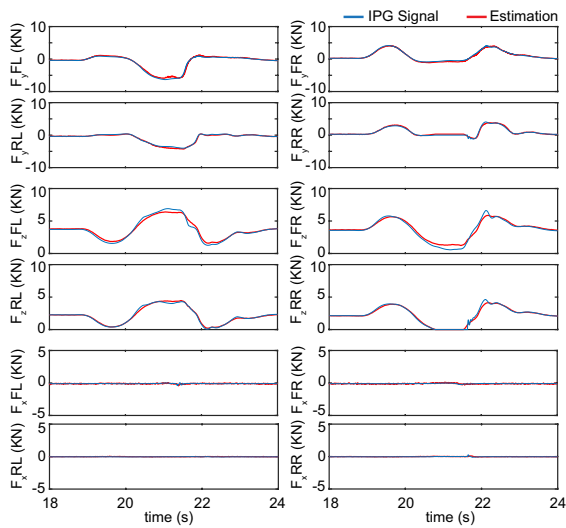


Figure 8: Lateral (F_y), Vertical (F_z), and Longitudinal (F_x) tire forces estimated during the simulation of the ADAC Lane Change Test.

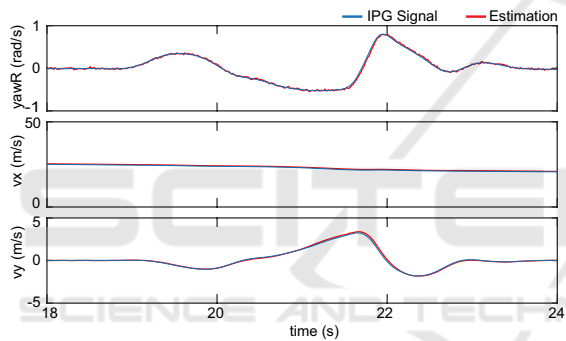


Figure 9: Yaw rate (ψ), longitudinal velocity (v_x), and lateral velocity (v_y) estimated during the simulation of the ADAC Lane Change test.

lateral weight transfer is maximum and the axle roll stiffness may change due to the contribution of the bump stops. In addition, wheel lift is observed in the rear inner wheel ($F_{z,RR}$) at this point. The vehicle motion states computed by the *UKF* are presented in Fig. 9. Overall, the estimation of the lateral velocity is remarkable, and the large lateral slide that occurs during the second gate ($t \approx 20 - 22s$) is approximated by the observer with high accuracy.

The results obtained in the Braking-in-a-turn test (#4) are presented in Figures (10-11). In this test, the vehicle accelerates steadily following a left-handed turn ($R = 100m$). The estimation of the vehicle states is particularly difficult in these conditions due to the low dynamic content of the maneuver, and thus an insignificant error can contribute after some seconds to generate a large drift in the estimated signals. In this case, the latter issue is not observed, and the forces generated by the tires are approximated very well by

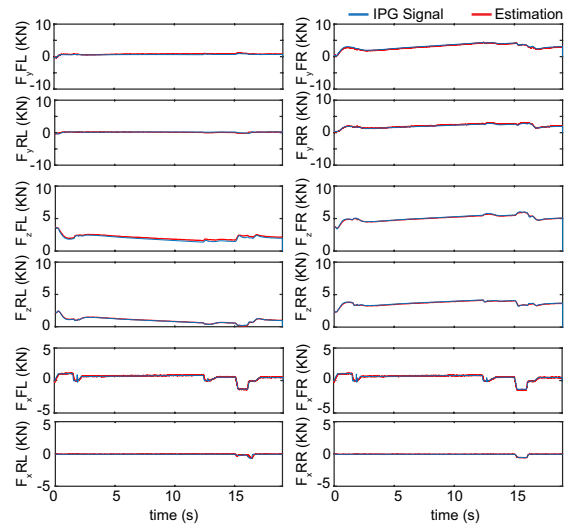


Figure 10: Tire forces estimated in the Braking-in-a-turn test.

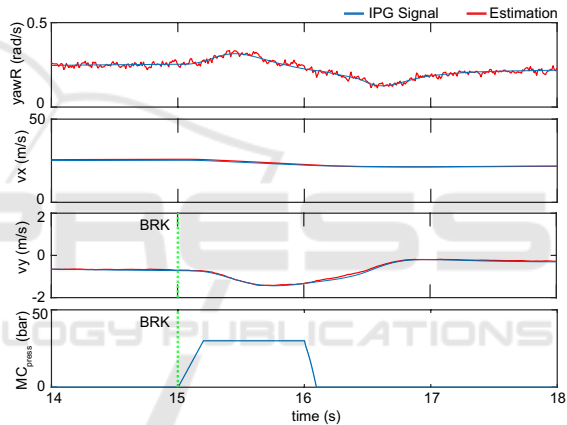


Figure 11: Vehicle motion states estimated in the Braking-in-a-turn test.

the virtual sensor. The tires of the outer side (front right, rear right) generate the majority of the lateral force due to the positive weight transfer. The longitudinal force estimates track well the gear shifting ($t \approx 2.5, t \approx 12.5$) events during the vehicle acceleration. At $t = 15s$, a partial braking input is introduced with the aim to excite the lateral dynamics and generate some instability in the vehicle. Due to the combination of high speed and high lateral force, the yaw damping of the vehicle is reduced in these circumstances, and the yaw dynamics exhibit an oscillatory response when the brakes are applied gently Fig. 11.

During the braking action, the lateral forces are diminished due to the force coupling, and the vehicle slides laterally to the outer side of the turn. In addition, the axle lateral forces do not decrease in the same proportion, and a slight overshoot in the yaw rate is observed. Overall, the precision of the *UKF* is

remarkable, and the lateral velocity is approximated accurately during the initial part of the test (steady-state) and after the application of the braking input (transient).

4.3 Metrics

Finally, in order to quantify numerically the precision of the virtual sensor, the normalized root means square (*NRMS*), expression (48), and the root means square (*RMS*) of the estimation error were computed for the tire forces and the vehicle states (Acosta et al., 2016; Doumiati et al., 2012).

$$e = 100 \frac{\sum_{k=1}^N \sqrt{(\hat{y}_k - y_k)^2}}{\max(|y|)} \frac{1}{N} \quad (48)$$

Where \hat{y}_k is the estimated signal and y_k is the real signal obtained from the simulation model. The numerical values corresponding to the vehicle states are provided in Table 5. The spaces corresponding to the *NRMS* have been left blank when the level of excitation is null and expression (48) presents a singularity.

Table 5: *NRMS* and *RMS* error of the vehicle states.

Test	$e_{\dot{\psi}}(\%)$	$e_{v_x}(\%)$	$e_{v_y}(\%)$
#1	-	1.59	-
#2	-	0.99	-
#3	1.63	1.04	1.31
#4	3.39	1.22	1.92
Test	$\sigma_{\dot{\psi}}(\text{rad/s})$	$\sigma_{v_x}(\text{m/s})$	$\sigma_{v_y}(\text{m/s})$
#1	0.01	0.63	0.02
#2	0.01	0.41	0.02
#3	0.01	0.28	0.04
#4	0.01	0.31	0.03

Table 6: *NRMS* and *RMS* error of the lateral forces.

Test	$e_{F_yFL}(\%)$	e_{F_yFR}	e_{F_yRL}	e_{F_yRR}
#1	-	-	-	-
#2	-	-	-	-
#3	2.42	2.88	2.52	3.34
#4	18.27	3.73	23.84	4.92
Test	$\sigma_{F_yFL}(N)$	σ_{F_yFR}	σ_{F_yRL}	σ_{F_yRR}
#1	72.34	73.56	152.33	86.59
#2	69.54	65.34	99.64	91.22
#3	153.14	119.18	101.31	135.47
#4	172.08	162.14	95.52	140.99

The states are accurately estimated by the *UKF*, and the *NRMS* values keep below the 5% threshold for all the tests performed. The errors of the individual tire lateral forces are presented in Table 6. Maximum *NRMS* values are seen in the tires of the inner

side (*FL*, *RL*) during the execution of the Braking-in-a-turn Test (#4). As these tires are unloaded and develop low lateral forces the *NRMS* metric tends to magnify the signal error. The accuracy of the virtual forces is very precise and values below the 5% threshold are observed in the forces generated by the outer tires. The errors obtained for the individual longitudinal tire forces are detailed in Table 7. Maximum *NRMS* errors are noticed during moments of low longitudinal excitation (e.g. coast down or free-rolling in the rear axle). When the longitudinal force is high (front axle during test #1, four wheels during test #2) the error level remains less than 10 percent.

Table 7: *NRMS* and *RMS* error of the longitudinal forces.

Test	$e_{F_xFL}(\%)$	e_{F_xFR}	e_{F_xRL}	e_{F_xRR}
#1	7.52	7.52	22.25	22.25
#2	5.34	5.35	3.66	3.81
#3	11.26	13.24	36.86	8.90
#4	6.68	6.63	7.69	2.30
Test	$\sigma_{F_xFL}(N)$	σ_{F_xFR}	σ_{F_xRL}	σ_{F_xRR}
#1	211.03	211.17	19.96	19.98
#2	204.93	205.02	39.90	41.47
#3	39.26	36.81	22.59	23.52
#4	90.18	90.03	55.12	12.93

Finally, the errors corresponding to the vertical tire forces are detailed in Table 8. Overall, the estimation errors are acceptable, and the open loop weight-transfer block performs well in both steady-state and transient situations.

Table 8: *NRMS* and *RMS* error of the vertical forces.

Test	$e_{F_zFL}(\%)$	e_{F_zFR}	e_{F_zRL}	e_{F_zRR}
#1	3.57	3.54	2.76	2.79
#2	3.13	3.10	4.37	4.34
#3	3.38	3.79	3.37	3.49
#4	5.28	1.39	2.54	1.89
Test	$\sigma_{F_zFL}(N)$	σ_{F_zFR}	σ_{F_zRL}	σ_{F_zRR}
#1	136.33	135.17	82.19	83.12
#2	171.59	169.95	113.19	112.39
#3	232.99	250.48	144.90	161.80
#4	192.67	84.07	61.70	79.13

The boxplots of the *NRMS* and *RMS* tire force errors are depicted in Fig. 12. The large whiskers show some dispersion in the *NRMS* error of the longitudinal and lateral forces due to the influence of the tests in which low excitation occur (e.g. longitudinal forces during *ADAC* lane change). Values found in the literature for the *NRMS* error range from 5% to 10% (Doumiati et al., 2012; Hamann et al., 2014), for Slalom and Lane Change maneuvers. In these works, additional assumptions such as the availability of a valid tire model (Doumiati et al., 2012), or the

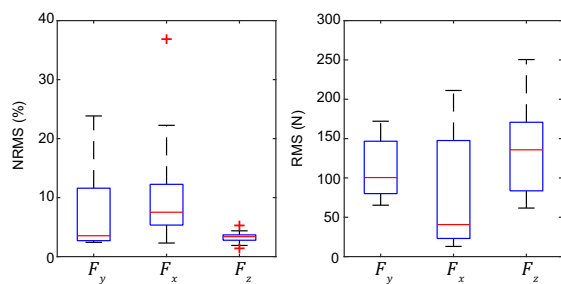


Figure 12: Box plots of the estimated tyre forces.

calculation of the lumped axle forces and the measurement of the longitudinal velocity (Hamann et al., 2014) have been considered. Error metrics have not been provided in other related works (Hrgetic et al., 2014), limiting the possibility of establishing a more detailed performance comparison.

5 CONCLUSIONS

In this paper, a virtual sensor to predict the friction forces developed by each tire and the principal vehicle planar states has been presented. Individual blocks to estimate the three-axis tire forces are integrated following a modular approach to form the complete state estimator structure. As tire model-less approaches are used in the observer, precise a priori knowledge about the tire friction characteristics is not necessary. A stochastic approach is used to estimate the tire forces in the longitudinal direction by means of a random-walk adaptive Linear Kalman filter, whereas a data-based approach is used to estimate the axle lateral forces. The nonlinear tire-road interactions in the lateral direction are captured by a Neural Networks structure. Finally, the individual tire lateral forces are obtained applying the vertical proportionality principle, and the tire normal forces necessary for this are computed using a steady-state open-loop observer.

An important contribution of this work is the use of adaptive covariance matrices to improve the performance of the Kalman Filters. A good trade-off between noise rejection and dynamic response is achieved in the random-walk Linear Kalman Filter using an adaptive process covariance matrix handled by a simple Fuzzy logic controller. Concerning the vehicle planar dynamics block, an adaptive measurement covariance matrix is employed in the Unscented Kalman filter to improve the accuracy of the longitudinal velocity inferred from the wheel speed, thus limiting the negative influence of the wheel speed fluctuations and avoiding the use of additional instrumentation (e.g. GPS).

The graphs and numerical results presented in this

paper demonstrate the remarkable performance of the virtual sensor under combined excitation in the longitudinal and lateral directions. Moreover, the state estimator approximates very well the vehicle states not only under high dynamic excitation but also during steady-state situations. The refinement of the vertical force estimation block in addition to an optimal tuning of the observer parameters using Swarm Intelligence algorithms will be pursued during the next stages of this research.

ACKNOWLEDGEMENTS

This project is part of the Interdisciplinary Training Network in Multi-Actuated Ground Vehicles (ITEAM) European program and has received funding from the European Unions Horizon 2020 research and innovation program under the Marie Skłodowska-Curie grant agreement No 675999. M. E. Fitzpatrick is grateful for funding from the Lloyds Register Foundation, a charitable foundation helping to protect life and property by supporting engineering-related education, public engagement and the application of research.

REFERENCES

- Acosta, M. and Kanarachos, S. (2016). Tire lateral force estimation and grip potential identification using neural networks, extended kalman filter, and recursive least squares. *Neural Computing and Applications, Springer*, pages 1–21.
- Acosta, M., Kanarachos, S., and Blundell, M. (2016). Agile maneuvering: From rally drivers to a finite state machine approach. In *IEEE Symposium Series on Computational Intelligence*.
- Albinsson, A., Bruzelius, F., Jonasson, M., and Jacobson, B. (2014). Tire force estimation utilizing wheel torque measurements and validation in simulations and experiments. In *Proceedings of the 12th International Symposium on Advanced Vehicle Control*.
- Antonov, S., Fehn, A., and Kugi, A. (2011). Unscented Kalman filter for vehicle state estimation. *Vehicle System Dynamics*, 49(9):1497–1520.
- Baffet, G., Charara, A., and Lechner, D. (2009). Estimation of vehicle sideslip, tire forces and wheel cornering stiffness. *Control Engineering Practice*, 17:1255–1264.
- Belic, I. (2012). Neural networks and static modeling. *Recurrent Neural Networks and Soft Computing, Dr. Mahmoud ElHefnawi*.
- Bosch (2006). *Hochdrucksensor Produktinformation*.
- Chakraborty, I., P.Tsiotras, and Lu, J. (2011). Vehicle posture control through aggressive maneuvering for mit-

- igation of t-bone collision. In *IEEE Conference on Decision and Control*.
- Cho, W., Yoon, J., Yim, S., Koo, B., and Yi, K. (2010). Estimation of tire forces for application to vehicle stability control. *IEEE Transactions on Vehicular Technology*, 59(2):638–649.
- Doumiati, M., Charara, A., Victorino, A., and Lechner, D. (2012). *Vehicle Dynamics Estimation using Kalman Filtering*. Wiley-ISTE.
- Doumiati, M., Victorino, A., Charara, A., Baffet, G., and Lechner, D. (2008). An estimation process for vehicle wheel-ground contact normal forces. In *IFAC proceeding Volumes*.
- Doumiati, M., Victorino, A., Charara, A., and Lechner, D. (2009). Estimation of vehicle lateral tire-road forces: A comparison between extended and unscented kalman filtering. In *Control Conference (ECC)*.
- Gao, X. (2010). Nonlinear estimation of vehicle sideslip angle based on adaptive extended kalman filter. *SAE Technical Papers*.
- Gray, A., Gao, Y., Lin, T., Hedrick, K., Tseng, H., and Borrelli, F. (2012). Predictive control for agile semi-autonomous ground vehicles using motion primitives. In *American Control Conference*.
- Hamann, H., Hedrick, J., Rhode, S., and Gauterin, F. (2014). Tire force estimation for a passenger vehicle with the unscented kalman filter. In *IEEE Intelligent Vehicles Symposium*.
- Hrgetic, M., Deur, J., Ivanovic, V., and Tseng, E. (2014). Vehicle sideslip angle ekf estimator based on nonlinear vehicle dynamics model and stochastic tire forces modeling. *SAE International Journal of Passenger Cars - Mechanical Systems*.
- Hrgetic, M., Deur, J., Pavkovic, D., and Barber, P. (2011). Adaptive ekf-based estimator of sideslip angle using fusion of inertial sensors and gps. *SAE International Journal of Passenger Cars - Mechanical Systems*, 4(1):700–712.
- Kanarachos, S. (2012). A new min-max methodology for computing optimised obstacle avoidance steering maneuvers of ground vehicles. *International Journal of Systems Science*, (45):1042–1057.
- Kanarachos, S., Griffin, J., and Fitzpatrick, M. (2016). Efficient truss optimization using the contrast-based fruit fly optimization algorithm. *Computers and Structures*, (182):137–148.
- Kiencke, U. and Nielsen, L. (2005). *Automotive Control Systems: For engine, driveline, and Vehicle*. Springer.
- Klier, W., Reim, A., and Stapel, D. (2008). Robust estimation of vehicle sideslip angle – an approach w/o vehicle and tire models. In *Proceedings of the SAE World Congress*.
- Pacejka, H. (2012). *Tire and Vehicle Dynamics*. Butterworth-Heinemann.
- Pylypchuk, V. and Chen, S. (2014). Tire force estimation with strain gauge measurement. In *ASME 2014 International Mechanical Engineering Congress and Exposition, IMECE*.
- RaceLogic (2015). *RLVBIMU04 Inertial Motion Unit Technical datasheet*. Racelogic.
- Rhudy, M. and Gu, Y. (2013). *Understanding Nonlinear Kalman Filters, Part II: An implementation Guide*. Interactive Robotics Letters, Tutorial.
- Velenis, A., Katzourakis, D., Frazzoli, E., Tsiotras, P., and Happee, R. (2011). Steady-state drifting stabilization of rwd vehicles. *Control Engineering Practice*, 19(11):1363–1376.
- Wan, E. A. and Van Der Merwe, R. (2000). The unscented kalman filter for nonlinear estimation. In *Adaptive Systems for Signal Processing, Communications, and Control Symposium*.
- Wenzel, T., Burnham, K., Blundell, M., and Williams, R. (2006). Dual extended kalman filter for vehicle state and parameter estimation. *Vehicle System Dynamics: International Journal of Vehicle Mechanics and Mobility*, 44:153–171.
- Young, P. (2011). *Recursive Estimation and Time-Series Analysis*. Springer.